Resonant Interactions and Chaotic Rotation of Pluto's Small Moons

M. R. Showalter[1] & D. P. Hamilton[2]

[1]SETI Institute, 189 Bernardo Avenue, Mountain View, CA 94043, USA.

[2]Department of Astronomy, University of Maryland, College Park, MD 20742, USA.

Four small moons—Styx, Nix, Kerberos and Hydra—follow near-circular, near-equatorial orbits around the central "binary planet" comprising Pluto and its large moon, Charon. New observational details of the system have emerged following the discoveries of Kerberos and Styx. Styx, Nix and Hydra are tied together by a three-body resonance, which is reminiscent of the Laplace resonance linking Jupiter's moons Io, Europa and Ganymede. However, perturbations by the other bodies inject chaos into this otherwise stable configuration. Nix and Hydra have bright surfaces similar to that of Charon. Kerberos, however, may be much darker, raising questions about how a heterogeneous satellite system might have formed. Nix and Hydra rotate chaotically, driven by the large torques of the Pluto-Charon binary. These results provide context for upcoming observations of the Pluto system by the New Horizons spacecraft in July 2015.

Pluto's moon Kerberos (previously designated "S/2011 (134340) 1" or, colloquially, "P4") was discovered in 2011[1] using images from the Hubble Space Telescope (HST). It orbits between the paths of Nix and Hydra, which were discovered in 2005 and confirmed in 2006[2]. Follow-up observations in 2012 led to the discovery of the still smaller moon Styx ("S/2012 (134340) 1" or "P5")[3]. The complete data set includes numerous additional detections of both objects from 2010–2012[4–6], plus a few detections from 2005 (Weaver, H. A., personal communication, 2011) and from 2006[7]; see Supplementary Table 1. Figure 1 shows samples of the available images. Motivated by these discoveries, we investigate the dynamics and physical properties of Pluto's four small outer moons.

Orbits

Pluto and Charon comprise a "binary planet"—two bodies, similar in size, orbiting their common barycenter. Their mutual motion creates a time-variable and distinctly asymmetric gravity field. This induces wobbles in the outer moons' orbits and also drives much slower apsidal precession and nodal regression[8]. In our analysis, we ignore the short-term wobbles and derive time-averaged orbital elements. This is equivalent to replacing the gravity field by that of two concentric rings containing the masses of Pluto or Charon, each with a radius equal to that body's distance from the barycenter.

We have modeled the orbits using six Keplerian orbital elements (semimajor axis a, eccentricity e, inclination i, mean longitude at epoch λ_0, longitude of pericenter ϖ_0 , and ascending node Ω_0) plus three associated frequencies (mean motion n, nodal precession rate $\dot{\varpi}$, and apsidal regression rate $\dot{\Omega}$). We work in the inertial "P-C" coordinate frame, with Pluto and Charon in the x-y plane and the z-axis parallel to the system's angular momentum pole (right ascension = 133.023°, declination = -6.218°)[6]. We have solved for these elements and frequencies under a variety of assumptions about how they are coupled (Extended Data Table 1). Table 1 lists the most robustly determined elements, in which we enforce a relationship that ensures $\dot{\varpi} \approx$ -$\dot{\Omega}$; this allows us to fit eight elements rather than nine. We prefer this solution because root-mean-square (RMS) residuals are nearly the same as for the solution where $\dot{\varpi}$ and $\dot{\Omega}$ are allowed to vary independently. Additional possible couplings, involving a and n as well, markedly increase the residuals for Styx and Nix; this suggests that non-axisymmetric gravitational effects, which are not modeled by our concentric ring approximation, can be important. The statistically significant (~ 100 km) residuals of Nix and Hydra (Table 1) match the predicted scale of the un-modeled wobbles[8], and so are to be expected.

Table 1 shows that e and i are distinctly nonzero; this was not apparent in prior work, which employed a different coordinate frame[5] or was based on 200-year averages[6]. Our results describe each moon's motion during 2005–2012 more accurately. Variations in n, e and i are detectable during 2010–2012 (Extended Data Fig. 1), illustrating the mutual perturbations among the moons that have been used to constrain their masses[6].

Search for Resonances

Pluto's five moons show a tantalizing orbital configuration: the ratios of their orbital periods are close to 1:3:4:5:6[1,3,5,9]. This configuration is reminiscent of the Laplace resonance at Jupiter, where the moons Io, Europa, and Ganymede have periods in the ratio 1:2:4. Table 1 shows orbital periods P of the moons relative to that of Charon, confirming the near-integer ratios. However, with measured values for $\dot{\varpi}$ and $\dot{\Omega}$ in addition to n, it becomes possible to search for more complicated types of resonances. A general resonance involves an angle $\Phi = \sum_j (p_j \lambda_j + q_j \varpi_j + r_j \Omega_j)$ and its time derivative $\dot{\Phi} = \sum_j (p_j n_j + q_j \dot{\varpi}_j + r_j \dot{\Omega}_j)$. Here, (p_j, q_j, r_j) are integer coefficients and each j subscript is C, S, N, K or H to identify the associated moon. A resonance is recognized by coefficients that sum to zero and produce a very small value of $\dot{\Phi}$; in addition, the resonant argument Φ usually librates around either 0° or 180°.

Using the orbital elements and their uncertainties tabulated in Table 1, we have performed an exhaustive search for strong resonances in the Pluto system. One dominant three-body resonance was identified: $\Phi = 3\lambda_S - 5\lambda_N + 2\lambda_H \approx 180°$. This defines a ratio of synodic periods: $3S_{NH} = 2S_{SN}$, where the subscripts identify the pair of moons. We find that $\dot{\Phi} = -0.007 \pm 0.001°/\text{day}$ and that Φ decreases from 191° to 184° during 2010–2012; this is all consistent with a small libration about 180°. Note that this expression is very similar to that for Jupiter's Laplace Resonance, where $\Phi_L = \lambda_I - 3\lambda_E + 2\lambda_G \approx 180°$ and $2S_{IE} = S_{EG}$. For comparison, Φ_L librates by only $\sim 0.03°$[10]. However, a similar resonant angle among the exoplanets of Gliese 876 librates about 0° by $\sim 40°$[11].

Using the current ephemeris and nominal masses[6], our numerical integrations indicate that Φ circulates, meaning that the resonance is inactive (Fig. 2). However, libration occurs if we increase the masses of Nix and Hydra, M_N and M_H, upward by small amounts (Fig. 3). Between these two limits, Φ varies erratically and seemingly chaotically. Extension of Fig. 3 to higher masses reveals that libration is favored but never guaranteed. By random chance, it would be unlikely to find Styx orbiting so close to a strong three-body resonance, and our finding that $\Phi \approx 180°$ increases the likelihood that this resonance is active. We therefore believe that $M_N + M_H$ has been slightly underestimated. The net change need not be large ($\lesssim 1 \sigma$)[6], and is also compatible with the upper limit on $M_N + M_H$ required for the long-term orbital stability of Kerberos[12].

Extended Data Fig. 2 shows that Kerberos contributes to the chaos. To understand its role, we perform simulations in which Pluto and Charon have been merged into one central body, thereby isolating the effects of the other moons on Φ. We perform integrations with $M_K = 0$ and with M_K nominal, and then Fourier transform $\Phi(t)$ to detect the frequencies of the perturbations (Extended Data Fig. 3). When M_K is nonzero, the power spectrum shows strong harmonics of the three synodic periods S_{SK}, S_{NK} and S_{KH}; this is because $\Phi(t)$ is a linear combination of $\lambda_S(t)$, $\lambda_N(t)$ and $\lambda_H(t)$, and Kerberos perturbs each moon during each passage. The harmonics of a second three-body resonance also appear: $\Phi' = 42\lambda_S - 85\lambda_N + 43\lambda_K \approx 180°$, i.e., $42S_{NK} \approx 43S_{SN}$. This was the second strongest resonance found in our search; at the orbit of Styx, the two resonances are separated by just 4 km. This is reminiscent of the Uranus system, where chains of near-resonances drive the chaos in that system[13,14].

These results will influence future models of Pluto system formation. Charon was probably formed by a large impact into Pluto[15], and the outer moons accreted from the leftover debris. If Charon had a large initial eccentricity, then its corotation resonances could lock material into the 1:3:4:5:6 relationship[16]. As Charon's eccentricity damped, the resonant strengths waned, but the moons were left with periods close to these integer ratios[17]. This appealing model has numerous shortcomings, however[18–20]. The presence of a strong Laplace-like resonance places a new constraint on formation models. Additionally, future models must account for the nonzero eccentricities and inclinations of the small satellites; for example, these might imply that the system was excited in the past by resonances that are no longer active[21,22].

The resonance enforces a modified relationship between orbits: if $P_N/P_C = 4$ and $P_H/P_C = 6$, then $P_S/P_C = 36/11 \approx 3.27$. Nevertheless, the other three near-integer ratios remain unlikely to have arisen by chance. Excluding Styx, the probability that three real numbers would all fall within 0.11 of integers is just 1%.

Shapes, Sizes and Physical Properties

Mean disk-integrated photometry for each moon is listed in Table 1. To infer the sizes of these bodies, we also require their geometric albedos p_v. Charon is a relatively bright, with $p_v \approx$

38%. Kuiper Belt objects (KBOs) exhibit a large range of albedos, but the smallest KBOs tend to be dark; $p_v \approx$ 4–8% is common[23–26].

The photometry is expected to vary with phase angle α and, if a body is elongated or has albedo markings, with rotational phase. Extended Data Fig. 4 shows the raw photometry for Nix and Hydra. In spite of the otherwise large variations, an opposition surge is apparent for $\alpha \lesssim$ 0.5°; this is often seen in phase curves and is indicative of surface roughness. After dividing out the phase function model, Fig. 4 shows our measurements vs. orbital longitude relative to Earth's viewpoint. The measurements of Nix show no obvious pattern, suggesting that it is not in synchronous rotation; this is discussed further below.

With unknown rotation states, we can only assess the light curves in a statistical sense. We proceeded with some simplifying assumptions. (1) Each moon is a uniform triaxial ellipsoid, with dimensions $(a_{100}, b_{100}, c_{100})$, assuming $p_v = 100\%$. (2) Each measurement was taken at a randomly chosen, unknown rotational phase. (3) Each moon was in fixed rotation about its short axis. (4) The pole orientation may have changed during the gap in coverage between years; this is consistent with Supplementary Video 1, in which the rotation poles are generally stable for months at a time. We therefore describe the orientation by three values of sub-Earth planetocentric latitude, ϕ_{2010}, ϕ_{2011}, and ϕ_{2012}. We used Bayesian analysis to solve for the six parameters that provide the best statistical description of the data; see the Methods section for details.

Nix has an unusually large axial ratio of ~ 2:1 (Table 1), comparable to that of Saturn's extremely elongated moon, Prometheus. Hydra is also elongated, but probably less so. Also, Nix's year-by-year variations (Fig. 4) are the result of a rotation pole apparently turning toward the line of sight; this explains both its brightening trend and also the decrease in its variations during 2010–2012 (Extended Data Fig. 5). Pluto's sub-Earth latitude is 46°, so Hydra's measured pole is nearly compatible with the system pole. Nix's pole was ~ 20° misaligned in 2010 but may have reached alignment by 2012.

Given the inferred volume and an assumed albedo and density, we can estimate GM, where M is the mass and G is the gravitation constant. We consider four assumptions about the moons' physical properties, and compare GM to the dynamical estimates[6] (Table 1). Nix and Hydra are

probably bright, Charon-like objects; if they were darker, then *GM* would be too large to be compatible with upper limits on the masses[12].

Kerberos seems to be very different (Table 1). The dynamical inference that its mass is ~ 1/3 that of Nix and Hydra, yet it reflects only ~ 5% as much sunlight, implies that it is very dark. This violates our expectation that the moons should be self-similar, due to the ballistic exchange of regolith[27]. Such heterogeneity has one precedent in the Solar System: at Saturn, Aegaeon is very dark ($p_v < 15\%$), unlike any other satellite interior to Titan, and even though it is embedded within the ice-rich G ring[28]. The formation of such a heterogeneous satellite system is difficult to understand. Alternatively, the discrepancy would go away if the estimate of M_K is found to be high by ~ 2σ; this has a nominal likelihood of 16%. Further study is needed.

Rotation States

Nearly every moon in the solar system rotates synchronously; the only confirmed exception is Hyperion, which is driven into chaotic rotation by a resonance with Titan[29,30]. Neptune's highly eccentric moon Nereid may also rotate chaotically[31], but observational support is lacking[32,33]. We have searched for rotation periods that are consistent with the light curves of Nix and Hydra (Fig. 4), but results have been negative (Extended Data Fig. 6). Although we can sometimes find a rotation period that fits a single year's data (spanning 2–6 months), no single rotation period is compatible with all three years of data.

Dynamical simulations explain this peculiar result: a binary planet tends to drive its moons into chaotic rotation. This is illustrated in Fig. 5, showing the simulated rotation period and orientation of Nix vs. time. The moon has a tendency to lock into near-synchronous rotation for brief periods, but these configurations do not persist. At other times, the moon rotates at a period entirely unrelated to its orbit. Supplementary Video 1 provides further insights into the behavior; for example, it shows occasional pole flips, a phenomenon consistent with the observed changes in Nix's orientation. Lyapunov times are estimated to be a few months, or just a few times longer than the orbital periods. The time scale of the chaos depends on initial conditions and on assumptions about the axial ratios of the moons. The torques acting on a less elongated body such as Hydra are weaker, but nevertheless our integrations support chaos.

6

According to integrations spanning a few centuries, a moon that begins in synchronous rotation will stay there, albeit with large librations. It is therefore possible for synchronous rotation about Pluto and Charon to be stable. However, the large and regular torques of Pluto and Charon probably swamp the small effects of tidal dissipation within the moons, so they never have a pathway to synchronous lock.

Both photometry and dynamical models support the hypothesis that Nix and Hydra are in chaotic rotation. The mechanism is similar to that driving Hyperion's chaos, with Charon playing Titan's role. However, Titan's influence on Hyperion is magnified by a strong orbital resonance. For a binary such as Pluto-Charon, it appears to be a general result that non-spherical moons may rotate chaotically; no resonance is required.

Future Observations

The New Horizons spacecraft will fly past Pluto on July 14, 2015. At that time, many of the questions raised by this paper will be addressed. Although Kerberos will not be well resolved (2–3 km/pixel), images will settle the question of whether it is darker than the other moons. The albedos and shapes of Nix (imaged at $\lesssim 0.5$ km/pixel) and Hydra (at 1 km/pixel) will be very well determined. New Horizons will not obtain precise masses for the outer moons, but ongoing Earth-based astrometry and dynamical modeling will continue to refine these numbers, while also providing new constraints on the Laplace-like resonance. Because this resonance has a predicted libration period of centuries, the dynamical models will confirm or refute it long before a complete libration or circulation period can be observed.

Chaotic dynamics makes it is less likely to find rings or additional moons of Pluto. Within the Styx-Hydra region, the only stable orbits are coorbitals of the known moons. The region beyond Hydra appears to be the most likely region to find additional moons[17], although some orbits close to Pluto are also stable[34]. Independent of the new discoveries in store, we have already learned that Pluto hosts a rich and complex dynamical environment, seemingly out of proportion to its diminutive size.

1. Showalter, M. R. *et al*. New satellite of (134340) Pluto: S/2011 (134340). *IAU Circular* 9221 (2011).

2. Weaver, H. *et al*. Discovery of two new satellites of Pluto. *Nature* **439,** 943–945 (2006).

3. Showalter, M. R. et al. New satellite of (134340) Pluto: S/2012 (134340). *IAU Circular* 9253 (2012).

4. Weaver, H. A. *et al*. New satellite of (134340) Pluto: S/2011 (134340). *IAU Circular* 9221 (2011).

5. Buie, M. W., Grundy, W. M. & Tholen, D. J. Astrometry and orbits of Nix, Kerberos, and Hydra. *Astron. J.* **146**, (2013).

6. Brozović, M., Showalter, M. R., Jacobson, R. A., Buie, M. W. The orbits and masses of satellites of Pluto. *Icarus*, **246**, 317–329 (2015).

7. Steffl, A. J. *et al*. New satellite of (134340) Pluto: S/2011 (134340). *IAU Circular* 9221 (2011).

8. Lee, M. H. & Peale, S. J. On the orbits and masses of the satellites of the Pluto-Charon system. *Icarus* **184**, 573–583 (2006).

9. Buie, M. W. *et al*. Orbits and photometry of Pluto's satellites: Charon, S/2005 P1, and S/2005 P2. *Astron. J.* **132**, 290–298 (2006).

10. Sinclair, A. T. The orbital resonance amongst the Galilean satellites of Jupiter. *Mon. Not. Roy. Astron. Soc.* **171**, 59–72 (1975).

11. Rivera, E. J. *et al.* The Lick-Carnegie Exoplanet Survey: a Uranus-mass fourth planet for GJ 876 in an extrasolar Laplace configuration. *Astrophys. J.* **719**, 890–899 (2010).

12. Youdin, A. N., Kratter, K. M. & Kenyon, S. J. Circumbinary chaos: using Pluto's newest moon to constrain the masses of Nix and Hydra. *Astrophys. J.* **755**, 1–11 (2012).

13. Quillen, A. C. & French, R. S. Resonant Chains and Three-body Resonances in the Closely-Packed Inner Uranian Satellite System. *Monthly Notices Roy. Astron. Soc.* **445**, 3959–3986.

14. French, R. G., Dawson, R. I. & Showalter, M. R. Resonances, chaos, and short-term interactions among the inner Uranian satellites. *Astron. J.,* in press.

15. Canup, R. M. A giant impact origin of Pluto-Charon. *Science* **307,** 546-550 (2005).

16. Ward, W. R. & Canup, R. M. Forced resonant migration of Pluto's outer satellites by Charon. *Science* **313**, 1107–1109 (2006).

17. Kenyon, S. J. & Bromley, B. C. The formation of Pluto's low-mass satellites. *Astron. J.* **147**, 8–24 (2014).

18. Lithwick, Y. & Wu, Y. The effect of Charon's tidal damping on the orbits of Pluto's three moons. arXiv0802.2939L (2008).

19. Lithwick, Y. & Wu, Y. On the origin of Pluto's minor moons, Nix and Hydra. arXiv:0802.2951 (2013).

20. Levison, H. F. & Walsh, K. Forming the small satellites of Pluto. DPS meeting #45, #503.05 (2013).

21. Zhang, K. & Hamilton, D. P. Orbital resonances in the inner Neptunian system I. The 2:1 Proteus-Larissa mean-motion resonance. *Icarus* **188**, 386–399 (2007).

22. Zhang, K. & Hamilton, D. P. Orbital resonances in the inner Neptunian system II. Resonant history of Proteus, Larissa, Galatea, and Despina. *Icarus* **193**, 267–282 (2008).

23. Grundy, W. M., Noll, K. S. & Stephens, D. C. Diverse albedos of small trans-neptunian objects. *Icarus* **176,** 184–191 (2005).

24. Lykawka, P. S. & Mukai, T. Higher albedos and size distribution of large transneptunian objects. *Plan. Space Sci.* **53,** 1319–1330 (2005).

25. Stansberry, J. *et al.* Physical Properties of Kuiper Belt and Centaur Objects: Constraints from Spitzer Space Telescope. In *The Solar System beyond Neptune* (eds Barucci, M. A. *et al.*) 592 pp. (U. Arizona Press, 2007).

26. Lacerda, P. *et al.* The albedo–color diversity of transneptunian objects. *Astrophys. J. Lett.* **793**, L2 (2014).

27. Stern, S. A. Ejecta exchange and satellite color evolution in the Pluto system, with implications for KBOs and asteroids with satellites. *Icarus* **199**, 571–573 (2009).

28. Hedman, M. M., Burns, J. A. , Thomas, P. C., Tiscareno, M. S., & Evans, M. W. Physical properties of the small moon Aegaeon (Saturn LIII). *EPSC Abstracts* **6**, 531 (2011).

29. Wisdom, J., Peale, S. J. & Mignard, F. The chaotic rotation of Hyperion. *Icarus* **58**, 137–152 (1984).

30. Klavetter, J. J. Rotation of Hyperion. I-Observations. *Astron. J.* **97**, 570–579 (1989).

31. Dobrovolskis, A. R. Chaotic rotation of Nereid? *Icarus* **118**, 181–198 (1995).

32. Buratti, B. J., Gougen, J. D. & Mosher, J. A. No large brightness variations on Nereid. *Icarus* **126**, 225–228 (1997).

33. Grav, T., Holman, M. J. & Kavelaars, J. J. The short rotation period of Nereid. *Astrophys. J. Lett.* **591**, L71 (2003).

34. Giuliatti-Winter, S. M., Winter, O. C., Vieira Neto, E. & Sfair, R. Stable regions around Pluto. *Mon. Not. Roy. Astron. Soc.* **430**, 1892–1900 (2013).

Supplementary Information is available in the online version of the paper.

Author Contributions. M.R.S. performed all of the astrometry, photometry, orbit fitting and numerical modeling discussed herein. D.P.H. was co-investigator on the Kerberos discovery and has participated in the dynamical interpretations of all the results.

Author Information. Reprints and permissions information is available at www.nature.com/reprints. The authors declare no competing financial interests.

Correspondence and requests for materials should be addressed to M.R.S. (mshowalter@seti.org).

Table 1 | Derived properties of the moons

Property	Styx	Nix	Kerberos	Hydra
a (km)	42,656 ± 78	48,694 ± 3	57,783 ± 19	64,738 ± 3
λ_0 (°)	276.856 ± 0.096	63.866 ± 0.006	94.308 ± 0.021	197.866 ± 0.003
n (°/day)	17.85577 ± 0.00024	14.48422 ± 0.00002	11.19140 ± 0.00005	9.42365 ± 0.00001
e (10^{-3})	5.787 ± 1.144	2.036 ± 0.050	3.280 ± 0.200	5.862 ± 0.025
ϖ_0 (°)	296.1 ± 9.4	221.6 ± 1.4	187.6 ± 3.7	192.2 ± 0.3
$\dot{\varpi}$ (°/day)	0.506 ± 0.014	0.183 ± 0.004	0.115 ± 0.006	0.070 ± 0.001
i (°)	0.809 ± 0.162	0.133 ± 0.008	0.389 ± 0.037	0.242 ± 0.005
Ω_0 (°)	183.4 ± 12.5	3.7 ± 3.4	225.2 ± 5.4	189.7 ± 1.2
$\dot{\Omega}$ (°/day)	-0.492 ± 0.014	-0.181 ± 0.004	-0.114 ± 0.006	-0.069 ± 0.001
P (days)	20.16155 ± 0.00027	24.85463 ± 0.00003	32.16756 ± 0.00014	38.20177 ± 0.00003
P/P_C	3.156542 ± 0.000046	3.891302 ± 0.000004	5.036233 ± 0.000024	5.980963 ± 0.000005
RMS (σ)	1.44	2.59	1.27	2.77
RMS (mas)	17.8	4.22	11.2	3.21
RMS (km)	397	94	248	72
A (km^2)	14 ± 4	470 ± 75	29 ± 8	615 ± 55
R_{100} (km)	2.1 ± 0.3	12.2 ± 1.0	3.0 ± 0.4	14.0 ± 0.6
R_{38} (km)	3.4 ± 0.5	19.8 ± 1.6	4.9 ± 0.7	22.7 ± 1.0
R_{06} (km)	8.6 ± 1.2	50 ± 4	12.4 ± 1.7	57 ± 3
a_{100}/b_{100}		2.1 ± 0.6		1.7 ± 0.6
b_{100}/c_{100}		1.2 ± 0.2		1.2 ± 0.2
ϕ_{2010} (°)		25 ± 10		39 ± 16
ϕ_{2011} (°)		37 ± 15		46 ± 18
ϕ_{2012} (°)		46 ± 17		38 ± 16
V_{100} (km^3)	39 ± 17	5890 ± 1040	117 ± 49	8940 ± 1640
GM (10^{-3} km^3/s^2)	0.0 + 1.0	3.0 ± 2.7	1.1 ± 0.6	3.2 ± 2.8
Charon-like	0.018 ± 0.008	2.8 ± 0.5	0.06 ± 0.03	4.2 ± 0.8
Bright KBO	0.04 ± 0.02	6.2 ± 1.1	0.12 ± 0.05	9.4 ± 1.7
Median KBO	0.12 ± 0.05	17 ± 3	0.35 ± 0.14	26 ± 5
Dark KBO	0.26 ± 0.11	39 ± 7	0.78 ± 0.32	60 ± 11

Angles are measured from the ascending node of the P-C orbital plane on the J2000 equator. The epoch is UTC on July 1, 2011. Uncertainties are 1 σ. A = disk-integrated reflectivity; R_{100}, R_{38} and R_{06} are radius estimates assuming a spherical shape and p_v = 100%, 38%, and 6%; V_{100} is the ellipsoidal volume if p_v = 1. Estimates of $GM = G\,\rho\,p_v^{-3/2}\,V_{100}$ are shown for properties resembling those of Charon (density ρ = 1.65 g/cm^3; p_v = 0.38) and three types of KBOs: "bright" (ρ = 0.5; p_v = 0.1), "median" (ρ = 0.65; p_v = 0.06), and "dark" (ρ = 0.8; p_v = 0.04). Boxes enclose values within one sigma of the dynamical mass constraints[6].

Figure 1 | Example HST images of Pluto's small moons. (**a**) Kerberos detected May 18, 2005, in the Nix/Hydra discovery images. (**b**) Kerberos in the Nix and Hydra confirmation images, February 2, 2006. (**c**) A marginal detection of Styx, along with Kerberos, on March 2, 2006. (**d**) All four moons, June 25, 2010. (**e**) The Kerberos discovery image, June 28, 2011, with Styx also identified. (**f**) The Styx discovery image, July 7, 2011. All images were generated by coadding similar images and then applying an unsharp mask to suppress the glare from Pluto and Charon.

Figure 2 | Numerical integrations of the Styx-Nix-Hydra resonance. Resonant angle Φ is plotted vs. time, using three assumptions for the GM_H: 0.0032 (**a**), 0.0039 (**b**), and 0.0046 km^2/s^3 (**c**); these values are equivalent the nominal mass, a 0.25σ increase, and a 0.5σ increase[6]. $GM_N =$ 0.0044 km^2/s^3 throughout, equivalent to 0.5σ above its nominal mass. The modest increase in the M_H is sufficient to force a transition of Φ from circulation (Styx outside resonance) to libration (Styx locked in resonance).

Figure 3 | Mass-dependence of the Laplace-like resonance. The shade of each square indicates whether the associated pair of mass values produces circulation (black) or libration (white) during a 10,000 year integration. The moon masses M_H and M_N are each allowed to vary from nominal to nominal $+ 1\sigma$[6]. M_K is nominal. Shades of gray define transitional states: light gray if Φ is primarily circulating; dark gray if Φ is primarily librating; medium gray for intermediate states. The transition between black and white is not monotonic, suggesting a fractal boundary.

Figure 4 | Normalized light curves. Disk-integrated photometry and 1-σ uncertainties for (**a**) Nix and (**b**) Hydra have been normalized to $\alpha = 1°$ and then plotted as a function of projected orbital longitude. Here 0° corresponds to inferior conjunction with Pluto as seen from Earth. Measurements are color coded by year: red = 2010; green = 2011; blue = 2012. A tidally locked moon would systematically brighten at maximum elongation (90° and 270°).

Figure 5 | Numerical simulations of Nix's rotation. (**a**) The instantaneous rotation period is compared to the synchronous rate (dashed line). (**b**) The orientation is described by the angle

between Nix's long axis and the direction toward the barycenter. Nix librates about 0° or 180° for periods of time, but it jumps out of these states frequently.

Extended Data Figure 1 | Variations in orbital elements by year. Changes in (**a**) mean motion, (**b**) eccentricity, and (**c**) inclination are shown during 2010–2012 for Nix (red), Kerberos (green) and Hydra (blue). Vertical bars are ± 1 σ. Each individual point is a fit to a single year of data (cf. Extended Data Table 1). In (**a**), Δn is the mean motion of each body minus its average during 2006–2012.

Extended Data Figure 2 | The role of Kerberos in the Laplace-like resonance. We have initiated an integration with Styx exactly in its resonance with Nix and Hydra, and then have allowed it to evolve for 10,000 years. The diagrams are for (**a**) M_K nominal, (**b**) M_K reduced by 1 σ, (**c**) $M_K = 0$. The amplitude of the libration is stable when Kerberos is massless, but shows erratic variations otherwise.

Extended Data Figure 3 | Spectral signatures of Kerberos. We merge Pluto and Charon into a single central body and integrate $\Phi(t)$ for Styx in exact resonance. The power spectrum for $M_K = 0$ (light gray) obscures the same spectrum for M_K is nominal. Unobscured spikes are caused by Kerberos. (**a**) The impulses of Kerberos passing each moon create a signature at the synodic period and its overtones: $S_{SK} = 53.98$ days (green); $S_{NK} = 109.24$ days (red); $S_{KH} = 203.92$ days (blue). (**b**) Harmonics of the second resonance, with period $42S_{NK} \approx 43S_{SN} \approx 4590$ days, are also visible. The 3/2 harmonic is unexplained.

Extended Data Figure 4 | Satellite phase curves. Raw disk-integrated photometry has been plotted vs. phase angle α for (**a**) Nix and (**b**) Hydra. Vertical bars are ± 1 σ. An opposition surge is apparent. A simple parametric model for the phase curve is shown: $c \cdot (1 + d/\alpha)$, where d is fixed but c is scaled to fit each moon during each year. Measurements and curves are color coded by year: red = 2010; green = 2011; blue = 2012.

Extended Data Figure 5 | Distribution of photometric measurements by year. The black curves show the theoretical distribution of A by year for Nix (**a** = 2010; **b** = 2011; **c** = 2012) and Hydra (**d** = 2010; **e** = 2011; **f** = 2012), after convolution with the measurement uncertainties. The histogram of measurements from each year are shown in red. In spite of small number statistics, the measurements appear to be well described by the models, which have been derived via Bayesian analysis.

Extended Data Figure 6 | Searches for rotation periods in the light curves. We fitted a simple model involving a frequency and its first harmonic to the photometry (Eq. 10) of (**a**) Nix and (**b**) Hydra. Curves are plotted for data from 2010 (red), 2012 (blue) and for three years 2010–2012 (black). Local minima with RMS residuals $\lesssim 1$ indicate a plausible fit. The orbital periods and half-periods are identified; if either moon were in synchronous rotation, we would expect to see minima near either P (for albedo variations) or $P/2$ (for irregular shapes).

Extended Data Table 1 | Orbital elements based on coupling various orbital elements and based on subsets of the data. Columns M_1 and M_0 identify the numbers of measurements included in and excluded from the fit; N indicates the number of free parameters. When $N = 8$, we derived $\dot{\Omega}$ from the relationship $\nu^2 = 2n^2 - \kappa^2$. For $N = 7$, $\dot{\Omega}$ and $\dot{\varpi}$ were both derived from n and the gravity field using Eqs. 5b,c. For $N = 6$, a was also coupled to n via Eq. 5a. $N = 3$ indicates a fit to a circular orbit. For fits to single years of data, the epoch is July 1 UTC for that year. We disfavor $N \leq 7$ in the multi-year fits because some residuals increase significantly.

Methods

Data Selection and Processing

Our data set encompasses all available HST images of the Pluto system during 2006 and 2010–2012, plus Kerberos in 2005. We neglected HST observations from 2002, 2003, and 2007[5,10], because they are of generally lower quality, rendering Kerberos and Styx undetectable. We emphasized long exposures through broad-band filters, although brief exposures of Charon and Pluto provided geometric reference points. Supplemental Table 1 lists the images and bodies measured. We analyzed the calibrated ("flt") image files. To detect Kerberos and Styx, it was often necessary to align and coadd multiple images from the same visit; files produced in this manner are listed in the table with a "coadd" suffix.

We fitted a model point spread function (PSF) to each detectable body. The PSFs were generated using the "Tiny Tim" software maintained by the Space Telescope Science Institute (STScI)[35,36]. Upon fitting to the image, the center of the PSF provides the astrometry and the integrated volume under the 2-D curve, minus any background offset, is proportional to the disk-integrated photometry. We measured objects in order of decreasing brightness and subtracted each PSF before proceeding; this reduced the effects of glare on fainter objects. Measurements with implausible photometry were rejected; this was generally the result of nearby background stars, cosmic ray hits, or other image flaws. Further details of the analysis are provided elsewhere[6]. Styx photometry (Table 1) might be biased slightly upward by our exclusion of non-detections; however, photometry of the other moons is very robust.

The Pluto-Charon Gravity Field

We have simplified the central gravity field by taking its time-average. The resulting cylindrically symmetric gravity field can then be expressed using the same expansion in spherical harmonics that is traditionally employed to describe the field of an oblate planet:

$$V(r, \theta, \phi) = -GM/r \cdot [1 - \sum_{m=2}^{\infty} J_m \ (R/r)^m \cdot P_m(\sin \phi) \ ]. \qquad [1]$$

Here (r, θ, ϕ) are polar coordinates, where r is radius and θ and ϕ are longitude and latitude angles, respectively; G is the gravitation constant, M is the body's mass, R is its equatorial radius, P_m are the Legendre Polynomials, J_m are coefficients in the expansion. The dependence

on θ and the odd m-terms in the series vanish by symmetry. The coefficients J_m can be determined by noting that the potential along the axis of the ring simplifies considerably:

$$V(r, \phi=\pi/2) = -GM/r \cdot [1 + (R/r)^2]^{-1/2}. \qquad [2]$$

This can then be compared to the definition of Legendre Polynomials:

$$(1 - 2xt + t^2)^{-1/2} = \sum_{m=0}^{\infty} t^m P_m(x). \qquad [3]$$

Substituting $t = (R/r)$ and evaluating the expression for $x = 0$ yields:

$$V(r, \phi=\pi/2) = -GM/r \cdot \sum_{m=0}^{\infty} (R/r)^m P_m(0) . \qquad [4]$$

Noting that $P_m(1) = 1$ for all m, equations [1] and [4] can only be equal if the coefficients J_m are negatives of the Legendre Polynomials evaluated at zero: $J_2 = 1/2$, $J_4 = -3/8$, $J_6 = 5/16$, etc. Given this sequence of coefficients, we can determine n, $\dot{\varpi}$, and $\dot{\Omega}$ as a functions of semimajor axis a:

$$n^2(a) = GM/a^3 \cdot [1 - \sum_{m=2}^{\infty} (1 + m) J_m (R/a)^m P_m(0)]; \qquad [5a]$$

$$\kappa^2(a) = GM/a^3 \cdot [1 - \sum_{m=2}^{\infty} (1 - m^2) J_m (R/a)^m P_m(0)]; \qquad [5b]$$

$$\nu^2(a) = GM/a^3 \cdot [1 - \sum_{m=2}^{\infty} (1 + m)^2 J_m (R/a)^m P_m(0)]. \qquad [5c]$$

Here κ is the epicyclic frequency and ν is the vertical oscillation frequency. It follows that $\dot{\varpi}(a) = n(a) - \kappa(a)$ and $\dot{\Omega}(a) = n(a) - \nu(a)$. In practice, we treated n as the independent variable because it has the strictest observational constraints, and then derived a, $\dot{\varpi}$, and $\dot{\Omega}$ from it.

Orbit Fitting

We modeled each orbit as a Keplerian ellipse in the P-C frame, but with additional terms to allow for apsidal precession and nodal regression. Our model is accurate to first order in e and i; any second-order effects can be neglected because they would be minuscule compared to the precision of our measurements.

We also required an estimate for the location of the system barycenter in each set of images. Because HST tracking is extremely precise between consecutive images, the barycenter location was only calculated once per HST orbit. We solved for the barycenter locations first and then

held them fixed for subsequent modeling of the orbital elements. Barycenter locations were derived from the astrometry of Pluto, Charon, Nix and Hydra. We locked Pluto and Charon to the latest JPL ephemeris, PLU043[6]. We accounted for the offset between center-of-light and center-of-body for Pluto using the latest albedo map[37]. However, because the number of Pluto and Charon measurements is limited, we also allowed Nix and Hydra to contribute to the solution. For each single year 2006–2012, we solved simultaneously for the barycenter location in each image set and also for orbital elements of Nix and Hydra. For the detection of Kerberos in 2005, the only available pointing reference was Hydra, which we derived from PLU043. By allowing many measurements to contribute to our barycenter determinations, we could improve their quality but also limit any bias introduced by shortcomings of our orbit models. Derived uncertainties in the barycenter locations are much smaller than any remaining sources of error.

A nonlinear least-squares fitter indentified the best value for each orbital element and also the covariance matrix, from which uncertainties could be derived. However, as noted in Table 1 and Extended Data Table 2, our RMS residuals (equivalent to the square root of χ^2 per degree of freedom) exceed unity. For Styx and Kerberos, marginal detections probably contributed to the excess; for Nix and Hydra, we have identified the source as the un-modeled wobbles in the orbits. All uncertainty estimates have been scaled upward to accommodate these underestimates.

During the orbit fits, we rejected individual points with excessive residuals, based on the assumption that they were misidentifications or the results of poor PSF fits. Extended Data Table 1 lists values for the number of included (M_1) and rejected (M_0) measurements. Rejecting points, however, would bias our uncertainty estimates downward. We compensated by running Monte Carlo simulations in which we generated (M_0+M_1) gaussian distributed, 2-D random variables and then rejected the M_0 that fall furthest from the origin. The standard deviation among the remainder then gave us an estimate of the factor by which we might have inadvertently reduced our error bars. With this procedure, accidentally rejecting a small number of valid measurements would not bias the uncertainties.

We also explored the implications of making various assumptions of how the orbital elements are coupled (Extended Data Table 1). For the purposes of this paper, we have adopted the $N = 8$ solutions in which $\dot{\Omega}$ can be derived from n and $\dot{\varpi}$. This assumption is helpful because,

18

when e and i are small, the frequencies $\dot{\varpi}$ and $\dot{\Omega}$ are especially difficult to measure. By allowing them to be coupled, we obtained more robust results. Nevertheless, our expectation that $\dot{\varpi}$ and $\dot{\Omega}$ should be roughly equal in magnitude but opposite in sign has been well supported by most of our uncoupled, $N = 9$ fits.

Resonance Analysis

We have defined a general resonance using a set of integer coefficients (p_j, q_j, r_j). The strength of a resonance is

$$C(\mathbf{p},\mathbf{q},\mathbf{r}) \cdot \prod \mu_j \cdot \prod e_j^{|q_j|} \cdot \prod \sin^{|r_j|}(i_j) , \qquad [6]$$

where μ_j is the mass ratio of moon j to the mass of Pluto. The first product excludes the mass of the smallest moon involved, because a resonance can exist even if one moon is a massless test particle. The function C defines a strength factor; however, because it has no simple expression, we ignore it in this analysis except to note, qualitatively, that the strongest resonances tend to involve small coefficients and/or small differences between coefficients.

We performed an exhaustive search for all possible resonances involving up to four nonzero coefficients, with $|p_j| \leq 300$, $|q_j| \leq 4$, and $|r_j| \leq 4$. Symmetry dictates that the coefficients sum to zero and that $\sum_j r_j$ must be even[38]. Because Charon follows a circular, equatorial orbit, $q_C = r_C = 0$. We first identified possible resonances by $\dot{\Phi} < 0.1°/day$, and then followed up by evaluating Φ for each year. Sets of coefficients for which Φ values clustered near $0°$ or $180°$ were given preference. We also favored sets of coefficients that have simple physical interpretations, and where the absolute values were small and/or close to one another.

Orbital Integrations

Our orbit simulations employed the numeric integrator SWIFT[39,40]. We used PLU043[6] as our reference ephemeris; it provides state vectors (positions and velocities) for all the bodies in the system vs. time. For simplicity, we neglected bodies outside the Pluto system in most integrations. The Sun is the dominant external perturber, shifting the moons by a few tens of km, primarily in longitude, after one Pluto orbit of 248 years; this is < 1% of our orbital uncertainties.

Each integration must begin with initial state vectors and masses for each body. However, the state vectors and masses are closely coupled; any change to one mass requires that we adjust all of the state vectors in order to match the observed orbits. Ideally, this would be accomplished by re-fitting to all of the available astrometry, but that task is beyond the scope of this paper. To simplify the problem, we generated false astrometry derived directly from PLU043, but sampled at the times of all prior HST visits that detected one or more of the four outer moons. Such measurements date back to June 11, 2002[5,6,9]. For each set of assumed masses, we used a nonlinear least-squares fitter to solve for the initial state vectors that optimally matched this astrometry. A similar technique was used to model the affects of moon masses on the chaotic dynamics of the Uranus system[41]. This procedure guarantees that our numeric integrations will match the actual astrometry with reasonable accuracy, regardless of the masses assumed.

For a few numerical experiments, we investigated the consequences of placing Styx exactly into its Laplace-like resonance (Extended Data Figs. 2 and 3). We accomplished this by generating a different set of false astrometry, in which the position of Styx was derived from the requirement that $\Phi = 180°$ at all times.

Photometry

Our numerical simulations suggest that typical rotation periods for each moon are comparable to the orbital period, i.e., several weeks. Because this time scale is long compared to one or a few of HST's 95-minute orbits, we combined measurements obtained from single or adjacent orbits. In Supplementary Table 1, adjacent orbits are indicated by an orbit number of 2 or 3. Our photometry (Fig. 4 and Extended Data Fig. 4) is defined by the mean and standard deviation of all measurements from a single set of orbits.

We considered two simple models for the light curves described as reflectivity A vs. time t:

$$A_1(t) = c_0 + c_1 \sin(\omega t) + c_2 \cos(\omega t) \tag{7a}$$

$$A_2(t) = c_0 + c_1 \sin(\omega t) + c_2 \cos(\omega t) + c_3 \sin(2\omega t) + c_4 \cos(2\omega t) \tag{7b}$$

We then sought the frequency ω that minimizes residuals. Given the small number of measurements in individual years, it was inappropriate to attempt more sophisticated models. Results are shown in Extended Data Figure 6. For the data from 2010, we did identify

frequencies where the residuals are especially small, suggesting that we may have identified a rotation rate for that subset of the data. However, in no case does a frequency persist from 2010 to 2012.

Shape Modeling

We have described the axial orientation relative to the line of sight using sub-Earth planetocentric latitude ϕ. The hypothetical light curve of an ellipsoid is roughly sinusoidal; its projected cross section on the sky varies between extremes A_{min} and A_{max}. If $\phi = 0$, $A_{min} = \pi bc$ and $A_{max} = \pi ac$. If $\phi = 90°$, then $A_{min} = A_{max} = \pi ab$. More generally,

$$A_{min}(a,b,c,\phi) = \pi b \ (c^2 \cos^2\phi + a^2 \sin^2\phi)^{1/2} \tag{8a}$$

$$A_{max}(a,b,c,\phi) = \pi a \ (c^2 \cos^2\phi + b^2 \sin^2\phi)^{1/2} \tag{8b}$$

If ϕ is fixed and each measurement was obtained at a uniformly distributed, random rotational phase, then the conditional probability density function for a cross section A given A_{min} and A_{max} is:

$$P(A \mid A_{min}, A_{max}) \propto (1 - [(A - A_0) / \Delta A]^2)^{-1/2} \ , \tag{9}$$

where $A_0 \equiv (A_{max} + A_{min})/2$ and $\Delta A = (A_{max} - A_{min})/2$. In reality, each measurement A has an associated uncertainty σ. This has the effect of convolving P with a normal distribution $N(A,\sigma)$, with zero mean and standard deviation σ.

$$P[\sigma](A \mid A_{min}, A_{max}, \sigma) \propto (1 - [(A - A_0) / \Delta A]^2)^{-1/2} \otimes N(A,\sigma) \ , \tag{10}$$

where the $\otimes$ operator represents convolution.

However, simulations show that ϕ varies due to chaotic rotation driven by the central binary (Supplementary Video 1). To simplify this analysis, we have assumed that ϕ was fixed during each year during which we obtained data, but that changes may have occurred between years; this is generally consistent with time spans of our data sets (a few months per year) and the infrequency of large pole changes in the simulations. This leads us to define three unknowns ϕ_{2010}, ϕ_{2011}, and ϕ_{2012}. Because A_{min} and A_{max} depend only on $\sin^2\phi$ and $\cos^2\phi$, we replace unknowns ϕ by $S \equiv \sin^2\phi$ in our analysis.

We have a vector of independent measurements $\mathbf{A} = (A_0, A_1, ...)$ and uncertainties $\boldsymbol{\sigma} = (\sigma_0, \sigma_1, ...)$, so the joint, conditional probability of obtaining all our measurements is a product:

$$P(\mathbf{A} \mid a, b, c, S_{2010}, S_{2011}, S_{2012}) = \prod P[\sigma_k](A_k \mid A_{min}(a,b,c,S_{y[k]}), A_{max}(a,b,c,S_{y[k]})) ,\qquad [11]$$

where $y[k]$ is the year associated with measurement k. Instead, we seek the joint, conditional probability density function $P(a, b, c, S_{2010}, S_{2011}, S_{2012} \mid \mathbf{A})$. This is a problem in Bayesian analysis:

$$P(a, b, c, S_{2010}, S_{2011}, S_{2012} \mid \mathbf{A}) =$$

$$P(\mathbf{A} \mid a, b, c, S_{2010}, S_{2011}, S_{2012}) \cdot P(\mathbf{A}) / P(a, b, c, S_{2010}, S_{2011}, S_{2012}) \qquad [12]$$

Here $P(\mathbf{A})$ and $P(a, b, c, S_{2010}, S_{2011}, S_{2012})$ represent our assumed "prior probability" distributions for these quantities. We have no prior information about our measurements A_k, so we assume that they are uniformly distributed. The second prior can be broken down as

$$P(a, b, c, S_{2010}, S_{2011}, S_{2012}) = P(a, b, c) P(S_{2010}) P(S_{2011}) P(S_{2012}) \qquad [13]$$

because orientations are independent of shape and of one another. If the pole in each year is randomly distributed over 4π steradians, then $P(\phi) \propto \cos\phi$ and $P(S) \propto S^{-1/2}$.

We model our prior for the shape as $P(a, b, c) = P_1(u) P_2(v) P_3(w)$, where $u \equiv abc$; $v \equiv a/b$; and $w \equiv b/c$. This states that we will regard the ellipsoid's volume and its two axial ratios as statistically independent. We have assumed that $\log(u)$ is uniformly distributed rather than u itself, which implies $P_1(u) \propto 1/u$. Experience with other irregularly-shaped planetary objects suggests that large ratios a/b and b/c are disfavored, with values rarely exceeding 2. After a bit of experimentation, we adopted $P_2(v) \propto 1/v^3$ and $P_3(w) \propto 1/w^3$. Alternative but similar assumptions had little effect on our results.

The above equations provide a complete solution to the joint probability function $P(a, b, c, S_{2010}, S_{2011}, S_{2012})$. We solved for the complete 6-dimensional function, represented as a 6-D array. Quantities listed in Table 1 were derived as the mean and standard deviation of P along each of its six axes, with S converted back to ϕ. Extended Data Figure 5 compares the distribution of measurements by year with the reconstructed probability distributions.

Simulations of Rigid Body Rotation

The orientation of the ellipsoid can be defined by a unit quaternion: $\mathbf{q} = [\cos(\theta/2), \sin(\theta/2)\,\mathbf{u}]$ represents a rotation by angle θ about unit axis vector $\mathbf{u}$. The time-derivative $d\mathbf{q}/dt = [0, \boldsymbol{\omega}] \cdot \mathbf{q}/2$, where $\boldsymbol{\omega}$ is the spin vector. We used a Bulirsch-Stoer integrator to track $\mathbf{q}$, $d\mathbf{q}/dt$, $\mathbf{x}$ and $d\mathbf{x}/dt$, where $\mathbf{x}$ is the position of the ellipsoid relative to the barycenter. The forces and torques acting were defined by Pluto and Charon following fixed circular paths around the barycenter; this motion was pre-defined for the simulations, not integrated numerically. We derived $d^2\mathbf{x}/dt^2$ from the gravity force of each body on the ellipsoid. We also required the second derivative of $\mathbf{q}$: $d^2\mathbf{q}/dt^2 = [-|\boldsymbol{\omega}|^2/2, \boldsymbol{\alpha}] \cdot \mathbf{q}/2$, where $\boldsymbol{\alpha}$ is the time-derivative of $\boldsymbol{\omega}$. We related $\boldsymbol{\alpha}$ to the torque applied by Pluto and Charon on the ellipsoid:

$$\boldsymbol{\tau} = 3\,GM_P\,\mathbf{r}_P \times (\mathbf{I}\,\mathbf{r}_P) / |\mathbf{r}_P|^5 + 3\,GM_C\,\mathbf{r}_C \times (\mathbf{I}\,\mathbf{r}_C) / |\mathbf{r}_C|^5 \,, \qquad [14]$$

where $\mathbf{r}_k = \mathbf{x} - \mathbf{x}_k$ is the vector offset from each body center to the ellipsoid's center and $\mathbf{I}$ is the ellipsoid's moment of inertia tensor. In the internal frame of the ellipsoid, the moment of inertia tensor $\mathbf{I}_0$ is diagonal, with $I_{11} = M/5\,(b^2 + c^2)$, $I_{22} = M/5\,(a^2 + c^2)$, and $I_{33} = M/5\,(a^2 + b^2)$. It is rotated to the system coordinate frame via the rotation matrix $\mathbf{R}$, which can be calculated from $\mathbf{q}$: $\mathbf{I} = \mathbf{R}\,\mathbf{I}_0\,\mathbf{R}^T$. We then solve for $\boldsymbol{\alpha}$ via the relation $\boldsymbol{\tau} = \mathbf{I}\,\boldsymbol{\alpha} + \boldsymbol{\omega} \times \mathbf{I}\,\boldsymbol{\omega}$.

Code Availability

Portions of our software are available at https://github.com/seti/pds-tools. We have opted not to release the entire source code because it is built atop additional large libraries representing decades of development. Instead, we have documented our algorithms with sufficient detail to enable others to reproduce our results.

35. Krist, J. E., Hook, R. N. & Stoehr, F. 20 years of Hubble Space Telescope optical modeling using Tiny Tim. *Proc. of SPIE* **8127**, 1–16 (2011).

36. STScI. Observatory Support: Tiny Tim HST PSF Modeling. http://www.stsci.edu/hst/observatory/focus/TinyTim (2011).

37. Buie, M. W. et al. Pluto and Charon with the Hubble Space Telescope II. Resolving changes on Pluto's surface and a map for Charon. *Astron. J.* **139**, 1128–1143 (2010).

38. Hamilton, D. P. A comparison of Lorentz, planetary gravitational, and satellite gravitational resonances. *Icarus* **109**, 221–240 (1994).

39. Levison, H. F. & Duncan, M. J. The long-term dynamical behavior of short-period comets. *Icarus* **108,** 18–36 (1993).

40. Levison, H. F. SWIFT: A solar system integration software package. http://www.boulder.swri.edu/~hal/swift.html (2014).

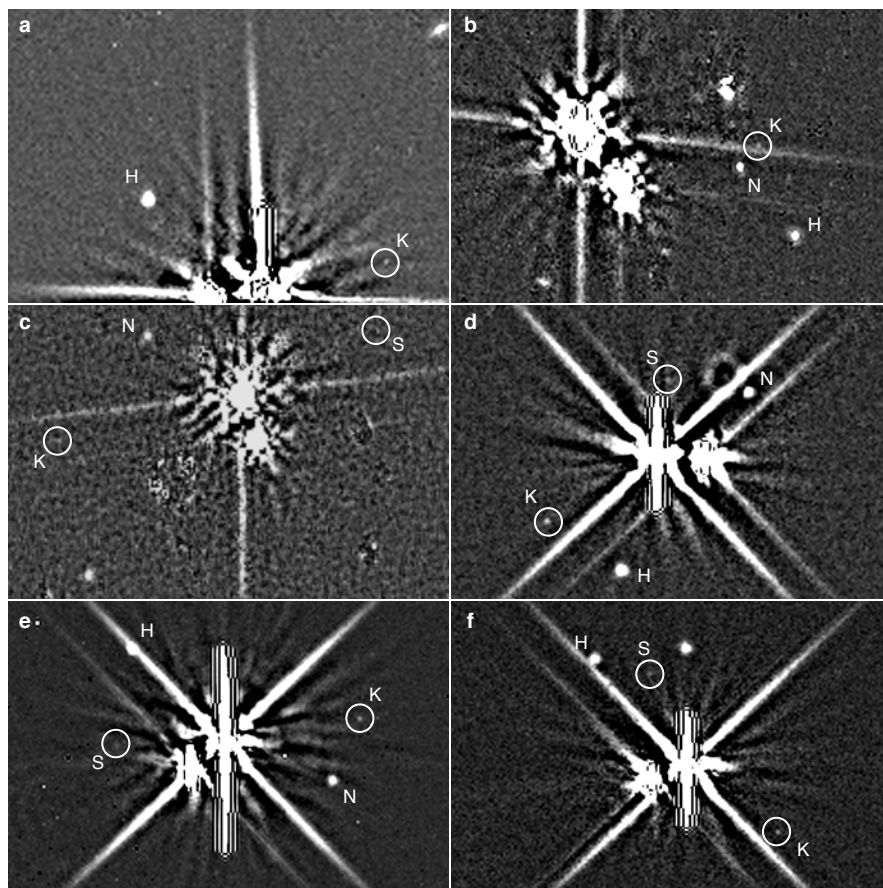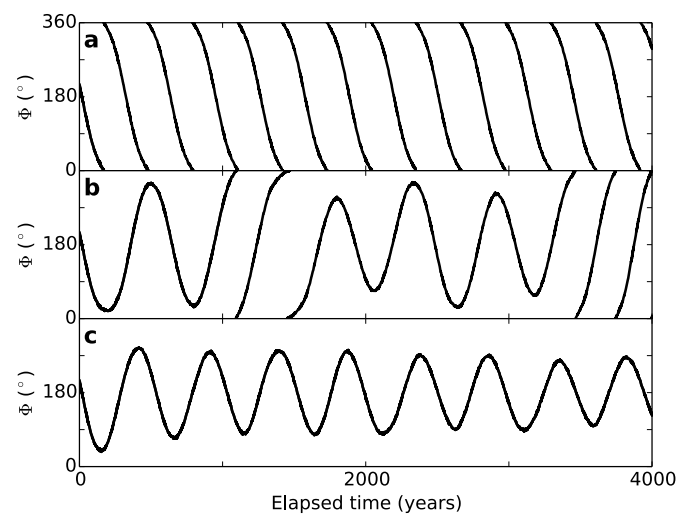41. French, R. S. & Showalter, M. R. Cupid is doomed: An analysis of the stability of the inner Uranian satellites. *Icarus* **220**, 911–921 (2012).
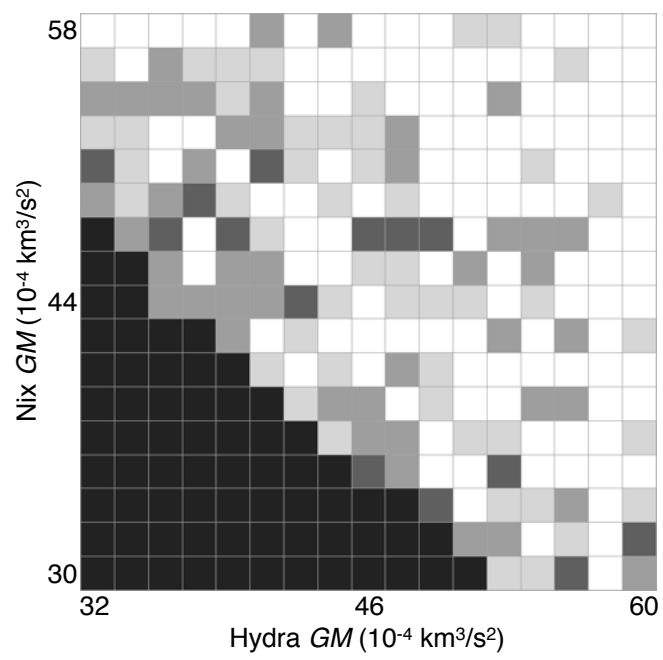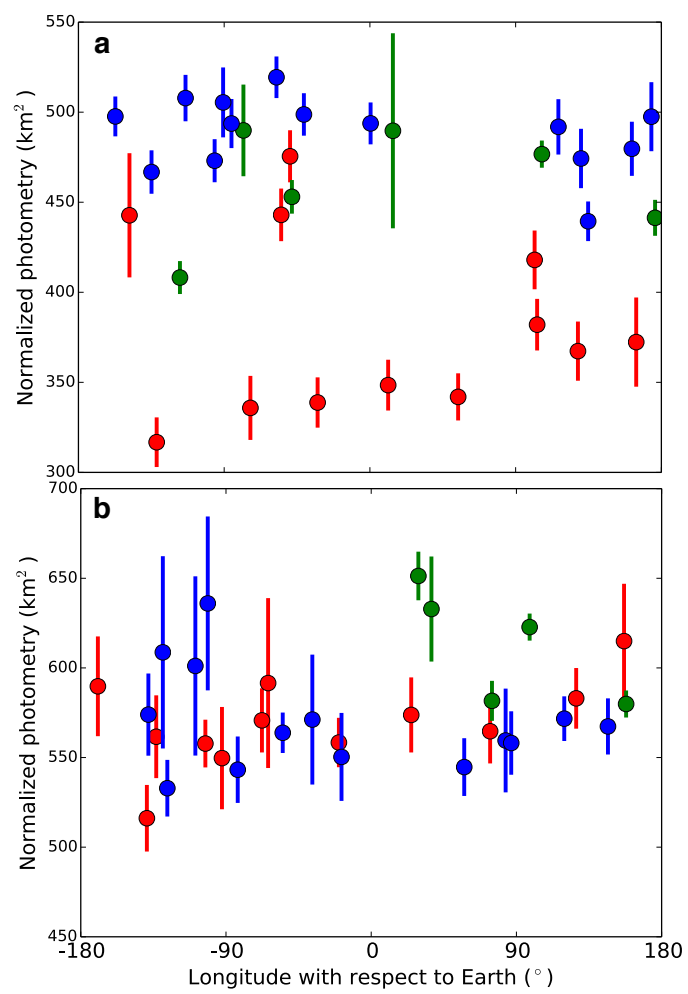
Figure 1

Figure 2

Figure 3

Figure 4
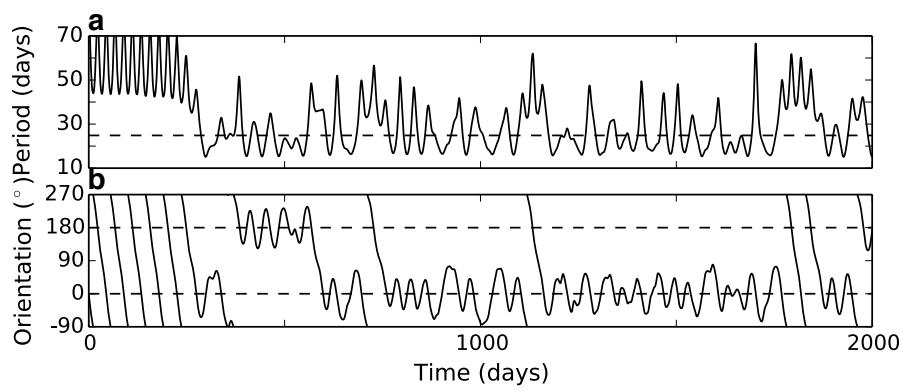
Figure 5

Extended Data Figure 1

Extended Data Figure 2

Extended Data Figure 3

Extended Data Figure 4

Extended Data Figure 5
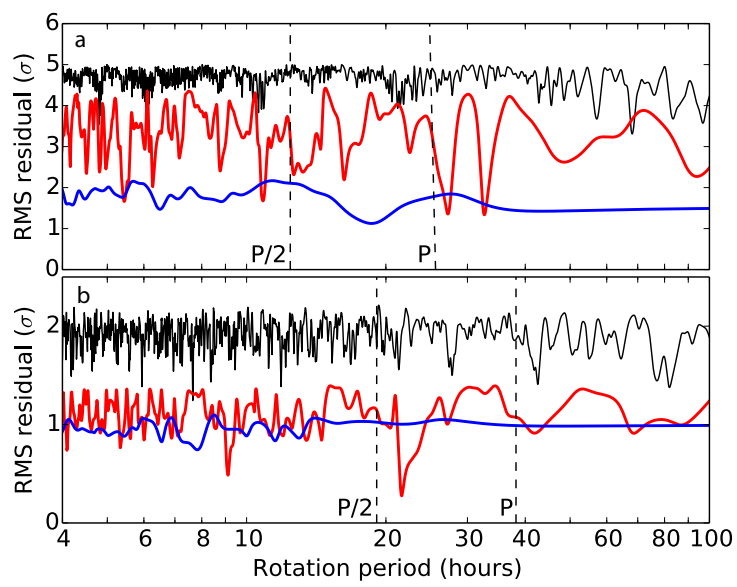
Extended Data Figure 6

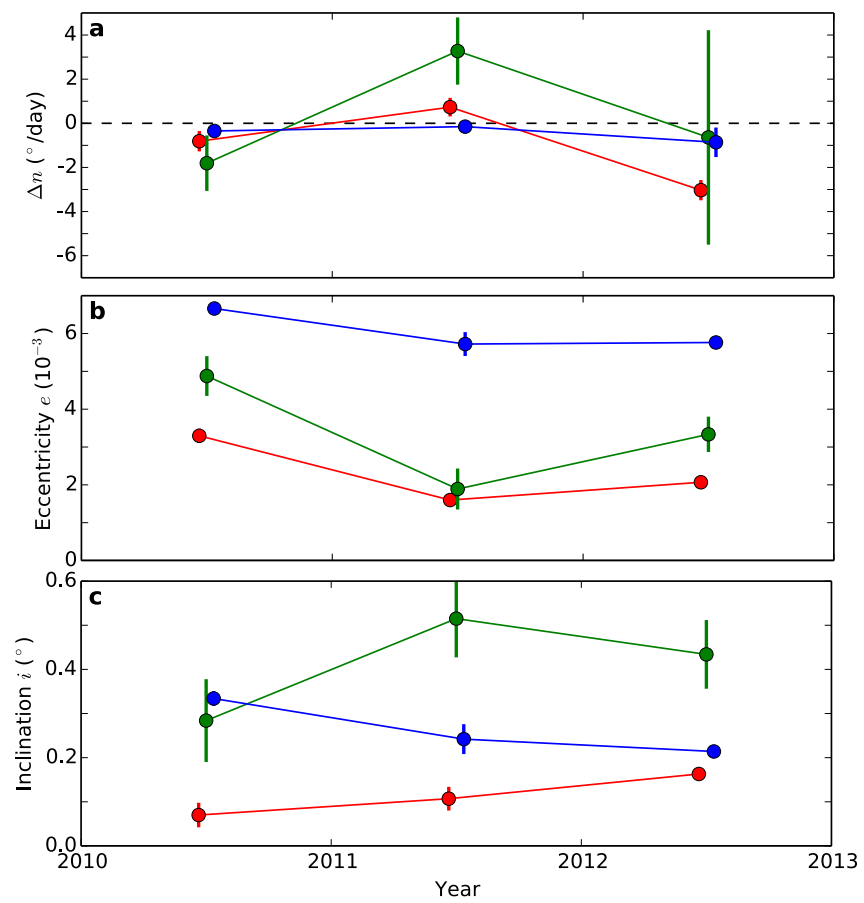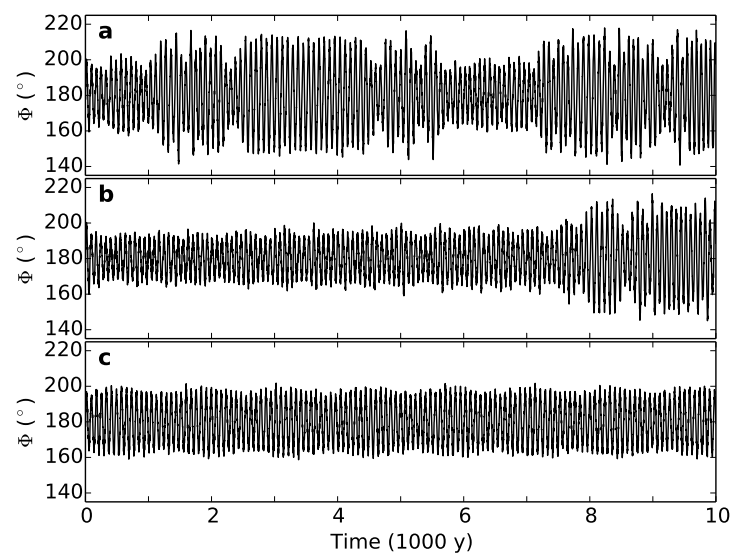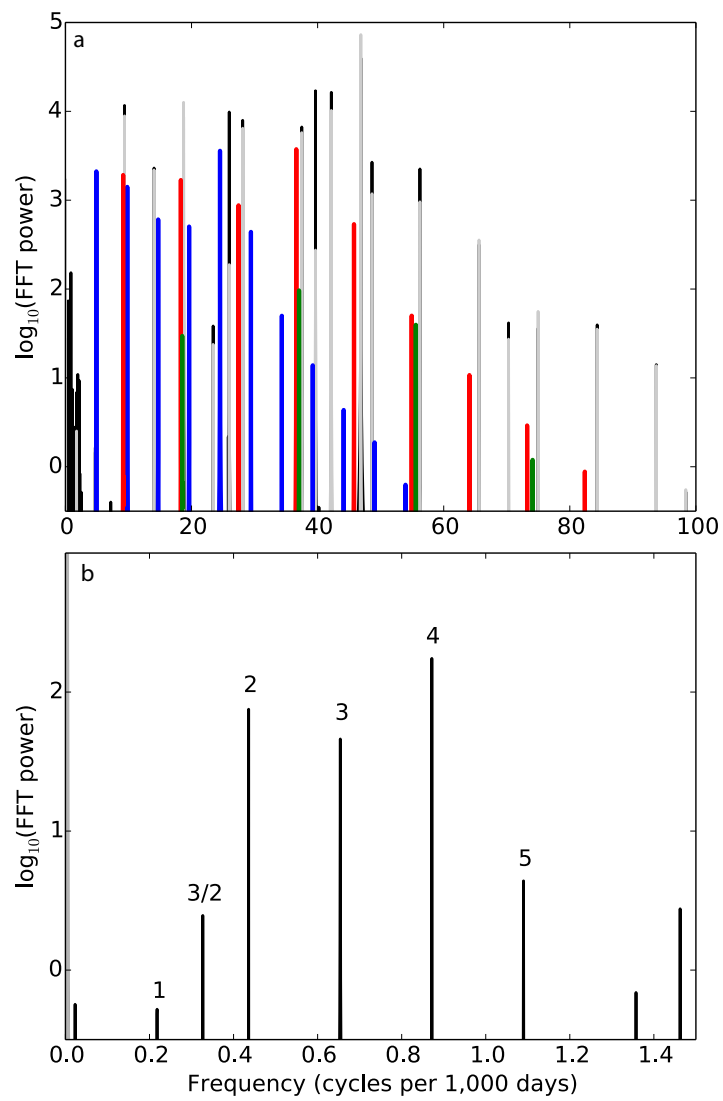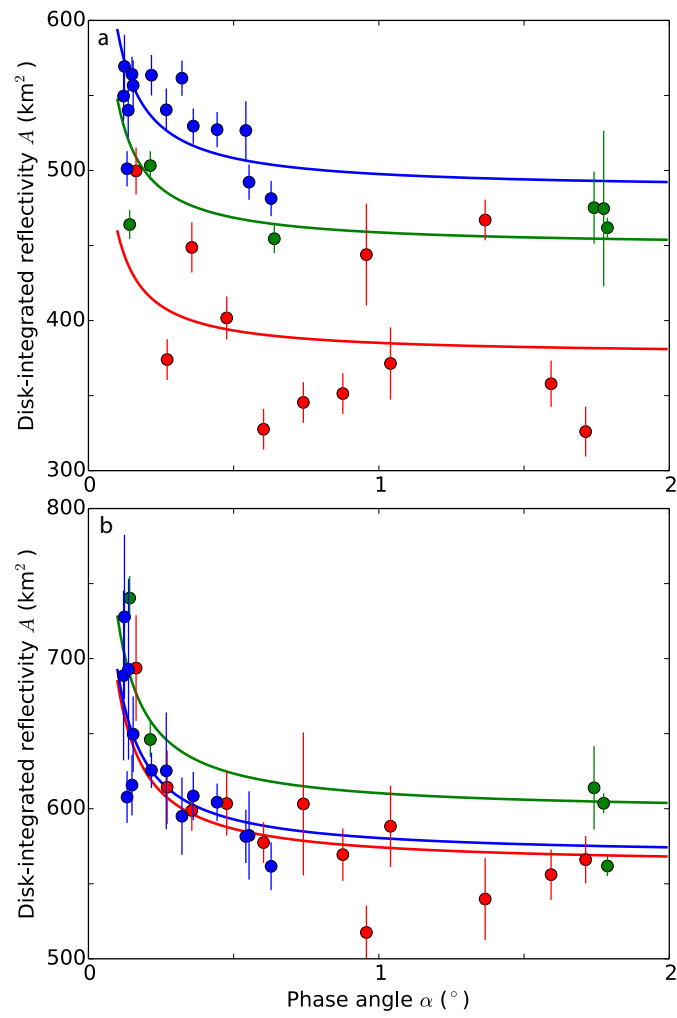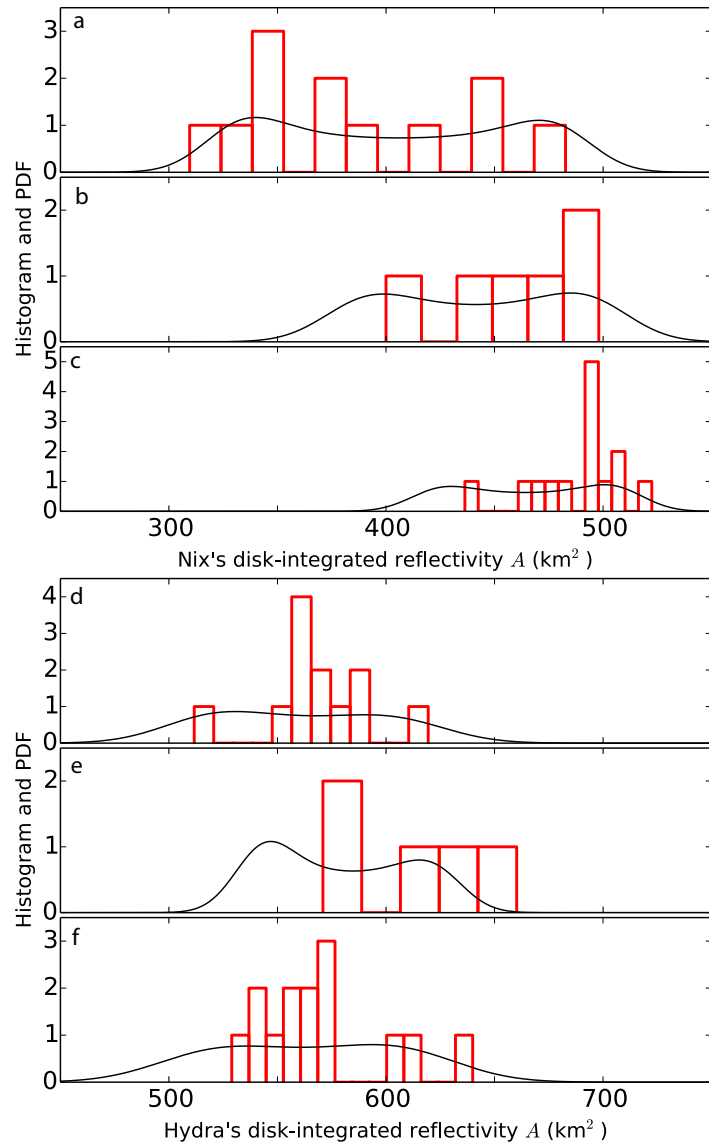| Moon	Years	N	a (km)	λ_0 (°)	n (°/day)	e (10^{-3})	ϖ_0 (°)	ϖ (°/day)	i (°)	Ω_0 (°)	$\dot{\Omega}$ (°/day)	P (days)	P/P_C	RMS (σ)	RMS (mas)	RMS (km)	M_1	M_0
Styx	2006–2012	9	42,662	276.8627	17.855814	5.892	296.15	0.49961	0.819	182.64	-0.50097	20.16150	3.156534	1.45	17.9	397	47	19
		±	81	0.0983	0.000255	1.179	9.49	0.02288	0.164	12.60	0.02376	0.00029	0.000050					
Styx	2006–2012	8	42,656	276.8562	17.855770	5.787	296.05	0.50581	0.809	183.36	-0.49187	20.16155	3.156542	1.44	17.8	397	47	19
		±	78	0.0955	0.000235	1.144	9.40	0.01405	0.162	12.50		0.00027	0.000046					
Styx	2006–2012	7	42,484	276.5918	17.855355	1.162	347.19	0.37688	0.381	176.10	-0.36908	20.16202	3.156615	1.79	19.3	429	47	19
		±	82	0.1046	0.000286	1.117	64.15		0.242	27.27		0.00032	0.000052					
Styx	2006–2012	6	42,422	276.5781	17.855333	1.054	7.70	0.37688	0.302	169.14	-0.36908	20.16204	3.156619	1.79	19.1	426	47	19
		±		0.1031	0.000285	1.102	65.26		0.215	33.76		0.00032	0.000052					
Styx	2010	7	43,549	239.9346	17.840396	7.733	138.44	0.37600	2.502	0.88	-0.36824	20.17892	3.159262	1.29	12.9	288	7	4
		±	617	0.2837	0.005338	2.225	16.61		0.894	13.64	0.00604	0.00604	0.000871					
Styx	2011	3	42,383	277.0515	17.807823								3.165041	1.10	16.1	363	12	1
		±		0.1879	0.018868								0.003818					
Styx	2012	7	42,856	332.3448	17.868293	6.915	116.85	0.37763	1.215	11.66	-0.36982	20.14742	3.154330	1.46	19.1	432	26	13
		±	117	0.2178	0.014056	1.712	11.95		0.297	13.73	0.01585	0.01585	0.003199					
Nix	2006–2012	9	48,697	63.8733	14.484221	2.022	220.27	0.19074	0.139	358.77	-0.15203	24.85463	3.891303	2.58	4.22	94	831	27
		±	3	0.0059	0.000015	0.050	1.41	0.00436	0.008	3.41	0.00842	0.00003	0.000004					
Nix	2006–2012	8	48,694	63.8655	14.484222	2.036	221.64	0.18325	0.133	3.73	-0.18096	24.85463	3.891302	2.59	4.25	95	831	27
		±	3	0.0056	0.000015	0.050	1.40	0.00409	0.008	3.40		0.00003	0.000004					
Nix	2006–2012	7	48,696	63.8580	14.484244	2.022	213.64	0.21395	0.133	15.03	-0.21084	24.85459	3.891296	2.65	4.35	97	831	27
		±	3	0.0054	0.000016	0.043	1.15		0.008	3.21		0.00003	0.000004					
Nix	2006–2012	6	48,693	63.8573	14.484240	2.030	213.40	0.21395	0.132	13.88	-0.21084	24.85460	3.891297	2.65	4.35	97	831	27
		±		0.0054	0.000016	0.041	1.13		0.008	2.89		0.00003	0.000050					
Nix	2010	7	48,670	177.1349	14.483409	3.297	146.01	0.21392	0.070	319.59	-0.21080	24.85603	3.891521	2.17	4.41	99	85	2
		±	10	0.0158	0.000385	0.143	2.37		0.024	20.48	0.00066	0.00066	0.000100					
Nix	2011	7	48,670	63.8130	14.484954	1.598	229.57	0.21398	0.107	352.81	-0.21086	24.85338	3.891106	2.75	5.22	117	124	11
		±	8	0.0187	0.000346	0.123	4.32		0.023	13.89	0.00059	0.00059	0.000094					
Nix	2012	7	48,704	325.0999	14.481191	2.068	292.10	0.21383	0.163	302.70	-0.21072	24.85983	3.892117	2.35	3.71	84	613	14
		±	4	0.0067	0.000382	0.060	1.27		0.011	3.51	0.00066	0.00066	0.000101					
Kerberos	2005–2012	9	57,832	94.3375	11.191287	3.471	186.59	0.12121	0.356	241.86	-0.20985	32.16788	5.036283	1.27	11.2	248	185	32
		±	20	0.0206	0.000063	0.209	3.58	0.00795	0.037	5.48	0.01302	0.00018	0.000030					
Kerberos	2005–2012	8	57,783	94.3078	11.191398	3.280	187.64	0.11536	0.389	225.15	-0.11419	32.16756	5.036233	1.26	11.2	249	185	32
		±	19	0.0211	0.000050	0.200	3.74	0.00615	0.037	5.43		0.00024	0.000024					
Kerberos	2005–2012	7	57,781	94.3074	11.191394	3.272	187.28	0.10957	0.385	225.17	-0.10851	32.16757	5.036234	1.27	11.3	251	185	32
		±	19	0.0214	0.000050	0.203	3.75		0.037	5.54		0.00014	0.000024					
Kerberos	2005–2012	6	57,750	94.3085	11.191397	3.221	187.86	0.10957	0.411	226.88	-0.10851	32.16756	5.036233	1.27	11.2	249	185	32
		±		0.0213	0.000050	0.199	3.79		0.035	4.86		0.00014	0.000024					
Kerberos	2010	7	57,825	329.5189	11.189590	4.877	140.09	0.10953	0.284	298.05	-0.10846	32.17276	5.037046	1.24	8.78	196	30	10
		±	48	0.0542	0.001181	0.481	5.69		0.090	17.99	0.00340	0.00340	0.000561					
Kerberos	2011	7	57,776	94.1883	11.194672	1.890	216.87	0.10965	0.515	250.03	-0.10859	32.15815	5.034760	1.19	6.99	157	30	1
		±	40	0.0680	0.001446	0.497	14.19		0.084	8.23	0.00415	0.00415	0.000652					
Kerberos	2012	7	57,803	230.3510	11.190758	3.335	233.57	0.10955	0.434	172.29	-0.10849	32.16940	5.036521	1.24	12.28	278	119	20
		±	38	0.0418	0.004783	0.423	8.24		0.074	8.23	0.01375	0.01375	0.002352					
Hydra	2006–2012	9	64,741	197.8685	9.423633	5.837	192.40	0.06842	0.244	191.15	-0.08762	38.20183	5.980972	2.73	3.19	71	835	24
		±	3	0.0032	0.000009	0.025	0.26	0.00081	0.005	1.19	0.00317	0.00003	0.000005					
Hydra	2006–2012	8	64,738	197.8662	9.423647	5.862	192.22	0.06986	0.242	189.67	-0.06934	38.20177	5.980963	2.77	3.21	72	835	24
		±	3	0.0032	0.000008	0.025	0.27	0.00080	0.005	1.17		0.00003	0.000005					
Hydra	2006–2012	7	64,738	197.8664	9.423645	5.861	192.04	0.07101	0.242	189.91	-0.07048	38.20178	5.980965	2.77	3.22	72	835	24
		±	3	0.0032	0.000008	0.025	0.24		0.005	1.15		0.00003	0.000005					
Hydra	2006–2012	6	64,721	197.8691	9.423638	5.881	192.04	0.07101	0.249	193.12	-0.07048	38.20181	5.980969	2.80	3.25	72	835	24
		±		0.0032	0.000008	0.025	0.24		0.005	0.99		0.00003	0.000005					
Hydra	2010	7	64,730	358.2681	9.423299	6.661	165.04	0.07101	0.334	219.90	-0.07048	38.20318	5.981184	2.77	3.07	69	85	2
		±	8	0.0079	0.000199	0.080	0.63		0.013	2.25	0.00081	0.00081	0.000124					
Hydra	2011	7	64,746	197.8686	9.423495	5.722	192.77	0.07101	0.242	193.93	-0.07048	38.20239	5.981060	2.88	3.24	73	135	12
		±	12	0.0166	0.000157	0.271	2.13		0.030	4.77	0.00064	0.00064	0.000088					
Hydra	2012	7	64,739	46.9262	9.422786	5.763	218.15	0.07100	0.214	157.81	-0.07047	38.20526	5.981510	2.35	2.93	66	606	10
		±	3	0.0033	0.000592	0.050	0.43		0.006	1.91	0.00240	0.00240	0.000379					

Extended Data Table 1